

Self-Assembly of a Monochromophore-Based Polymer Enables Unprecedented Ratiometric Tracing of Hypoxia

Shuwen Wang, Kaizhi Gu, Zhiqian Guo,* Chenxu Yan, Tingyuan Yang, Zhuo Chen, He Tian, and Wei-Hong Zhu*

The accuracy of traditional bischromophore-based ratiometric probes is always compromised by undesirable energy/charge transferring interactions between the internal reference moiety and the sensing chromophore. In this regard, ratiometric sensing with a monochromophore system is highly desirable. Herein, an unprecedented monochromophore-based ratiometric probe, which consists of a hydrophilic backbone poly(*N*-vinylpyrrolidone) (PVP) and single chromophore of platinum(II) tetraphenylporphyrin (Pt-TPP) is reported. Combination of the specific assembled clustering-triggered fluorescent emission (oxygen-insensitive) with the original Pt-TPP phosphorescence (oxygen-sensitive) enables successful construction of a monochromophore-based ratiometric nanosensor for directly tracing hypoxia *in vivo*, along with the preferable facilitation of enhanced permeation and retention effect and long excitation wavelength. The unique ratiometric signals enable the direct observation from normoxic to hypoxic environment in both living A549 cells and a tumor-bearing mice model, providing a significant paradigm of a monochromophore-based dual-emissive system with the specific assembled cluster emission. The work satisfactorily demonstrates a valuable strategy for designing monochromophore-based dual-emissive materials, and validates its utility for *in vivo* ratiometric biological sensing without the common energy/charge interference in bischromophore-based system.

Ratiometric optical imaging holds promise for noninvasive visualization of hypoxic microenvironment induced by cancer cells since it can provide real-time and accurate information on cancers from microscopic to macroscopic levels with built-in calibration.^[1] To date, a host of works on ratiometric optical imaging of tumor hypoxia rely on bischromophore-based system, which inevitably compromises imaging accuracy and specificity because of the undesirable energy/charge transferring interactions between the internal reference moiety and sensing chromophore (Scheme 1a).^[2] At present, the accurate diagnosis of cancer hypoxia via monochromophore-based sensor with ratiometric readout still remains challenging.^[3]

Nonconventional fluorescent biogenic and synthetic polymers without aromatic structures have recently attracted considerable attention, and their clusteroluminescence mechanism behind this abnormal phenomenon is increasingly deciphered.^[4] For instance, Tang and co-workers found that the intra- and inter-chain $n \rightarrow \pi^*$ interaction of carbonyl groups plays a crucial role during the

emission for oligo(maleic anhydride)s (OMAHs) in the aggregated state/condensed phase.^[5] Zhang and co-workers also proposed clustering-triggered emission mechanism, namely the clustering of nonconventional chromophores and subsequent electron cloud can overlap with the simultaneous rigidification of conformation in the process of poly(amino acids).^[4c] Thus, we examine whether the nonaromatic clusteroluminescence can be utilized as additional internal reference signal to construct a monochromophore-based ratiometric hypoxia nanosensor.

With this in mind, we borrowed the nonaromatic clusteroluminescence strategy and developed a monochromophore-based ratiometric hypoxia probe (Pt-TPP-PVP₄₃₀, Scheme 1b,c), which consists of a hydrophobic oxygen-sensitive Pt(II) tetraphenylporphyrin (Pt-TPP) and a hydrophilic backbone poly(*N*-vinylpyrrolidone) (PVP). Due to its amphiphilic nature, Pt-TPP-PVP₄₃₀ can self-assemble into nanoclusters in an aqueous solution, highly preferential to accumulate at tumor site by passive enhanced permeation and retention

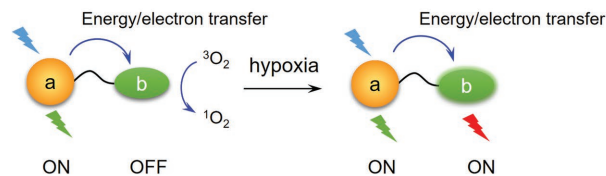
S. Wang, Dr. K. Gu, Prof. Z. Guo, Dr. C. Yan, Prof. H. Tian, Prof. W.-H. Zhu
Shanghai Key Laboratory of Functional Materials Chemistry
Key Laboratory for Advanced Materials and Institute of Fine Chemicals
Joint International Research Laboratory of Precision Chemistry and Molecular Engineering
Feringa Nobel Prize Scientist Joint Research Center
School of Chemistry and Molecular Engineering
East China University of Science and Technology
Shanghai 200237, China
E-mail: guozq@ecust.edu.cn; whzhu@ecust.edu.cn
T. Yang, Dr. Z. Chen
School of Pharmacy
East China University of Science and Technology
Shanghai 200237, China

 The ORCID identification number(s) for the author(s) of this article can be found under <https://doi.org/10.1002/adma.201805735>.

DOI: 10.1002/adma.201805735

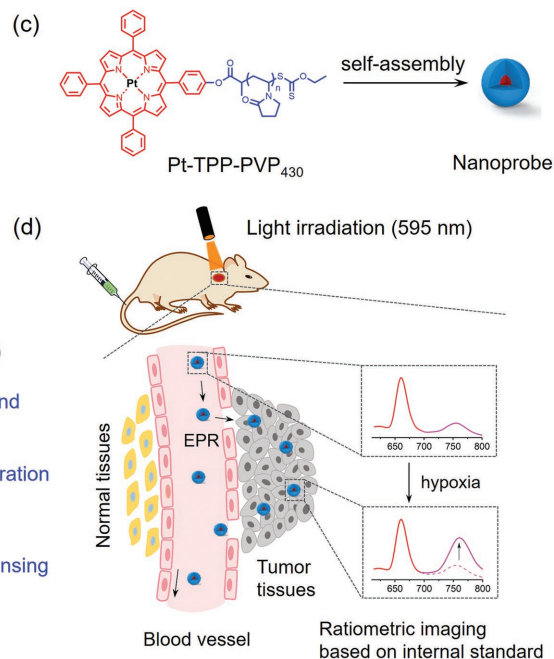
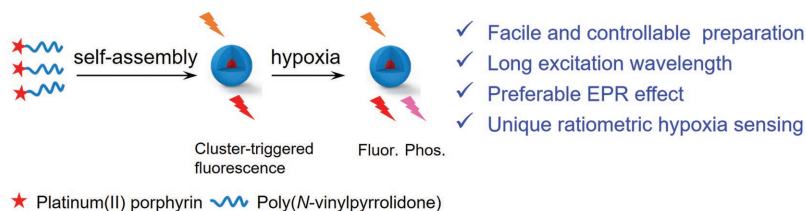
(a) Bischromophore-based ratiometric probes (signal $\propto I_b/I_a$)

Undesirable interactions: energy/electron transfer between two chromophores



(b) This work: Monochromophore-based ratiometric probe (signal $\propto I_{\text{fluor.}}/I_{\text{phos.}}$)

Avoiding interaction: using non-aromatic assembly fluorescence as internal standard



Scheme 1. Schematic representation of ratiometric hypoxia sensing. a) Bischromophore-based ratiometric probes by introducing an oxygen-insensitive dye as reference signal. b) Monochromophore-based ratiometric probe by using nonaromatic assembly fluorescence as internal standard. c) Chemical structure of amphiphilic nanosensor Pt-TPP-PVP₄₃₀. d) Ratiometric hypoxia sensing with micellar self-assembly nanosensor of Pt-TPP-PVP₄₃₀ via facilitation of EPR effect using the unique assembly clusteroluminescence as internal reference.

(EPR) effect. Significantly, the self-assembly nanosensor showcases a unique oxygen-insensitive near-infrared (NIR) fluorescent emission and oxygen-dependent phosphorescence signal, therefore making it particularly suitable for ratiometric quantification of tumor hypoxia in vivo (Scheme 1d). Furthermore, the as-prepared nanosensor bestows several striking characteristics such as long wavelength absorption, excellent storage/pH/photostability, as well as satisfactory biocompatibility. In contrast with the traditional bischromophore-based ratiometric system, our results demonstrate that self-assembly of monochromophore-based polymer enables a unique ratiometric assessment of hypoxia levels in living A549 cells and in vivo tumor-targeting bioimaging of hypoxia in mice model. To the best of our knowledge, the assembled cluster emission has been for the first time exploited as the unprecedented inner self-calibration for achieving ratiometric hypoxia sensing.

Given that PVP is a well-known nonionic macromolecular polymer with hydrophilicity, biocompatibility, and good stability in living tissues,^[6] we incorporated PVP chain into Pt-TPP for constructing the monochromophore-based Pt-TPP polymer (Pt-TPP-PVP₄₃₀) by reversible addition-fragmentation chain transfer polymerization with low-polydispersity indices (Scheme S1 and Table S1, Supporting Information). Due to the hydrophobicity of Pt-TPP and the hydrophilicity of PVP, the resulting amphiphilic polymer can spontaneously form micelles by self-assembly with an average diameter of 118 nm in aqueous solution, which was observed by dynamic light scattering (DLS) measurements (Figure 1a). This suitable nanoparticle size guarantees Pt-TPP-PVP₄₃₀ with a preferable EPR effect.^[7] Additionally, transmission electron microscopy (TEM) further confirmed

the spherical morphology with corresponding average diameter (Figure 1b). Time-dependent diameters of nanoparticles were monitored continuously by DLS measurement. As illustrated in Figure 1c, there are no obvious changes in diameter even after one month of storage at 25 °C, keeping aqueous dispersions of Pt-TPP-PVP₄₃₀ clear and stable. It exhibits a pale green color arising from its absorption band in visible light range (Figure 1d), along with high thermodynamic stability in aqueous solution.

Next, optical performances of Pt-TPP-PVP₄₃₀ were further systematically investigated. Compared with the ligand absorption spectra of TPP-PVP₄₃₀, the counterpart complex Pt-TPP-PVP₄₃₀ displayed a moderate absorption at ≈ 595 nm and a detectable blue-shift (15 nm) in the Soret-band region (Figure 2a). Interestingly, when Pt-TPP is coupled with PVP chain, a unique fluorescence from the aqueous self-assembly of Pt-TPP-PVP₄₃₀ was observed. Upon photoexcitation at 595 nm, not only did the assembled Pt-TPP-PVP₄₃₀ give an oxygen-sensitive phosphorescent emission up to ≈ 760 nm, but also exhibited another fluorescent emission band at 660 nm (Figures S1 and S2, Supporting Information). Here, the fluorescent emission at 660 nm was very dependent upon the specific assembly with efficient length of PVP chains, which might be resulted from the assembled clusters of the hydrophilic backbone PVP chain.^[8] The efficient length of PVP chains has two critical effects in Pt-TPP-PVP_n ($n \geq 200$): i) generation of cluster-induced fluorescent emission at 660 nm; ii) making the Pt-porphyrin phosphorescent emission shift from 655 to 760 nm (Figures S3–S5, Supporting Information). In addition, the observed fluorescent emission at 660 nm and phosphorescent emission at 760 nm in the system of Pt-TPP-PVP₄₃₀ were further verified by the fluorescence decay experiments. The unique

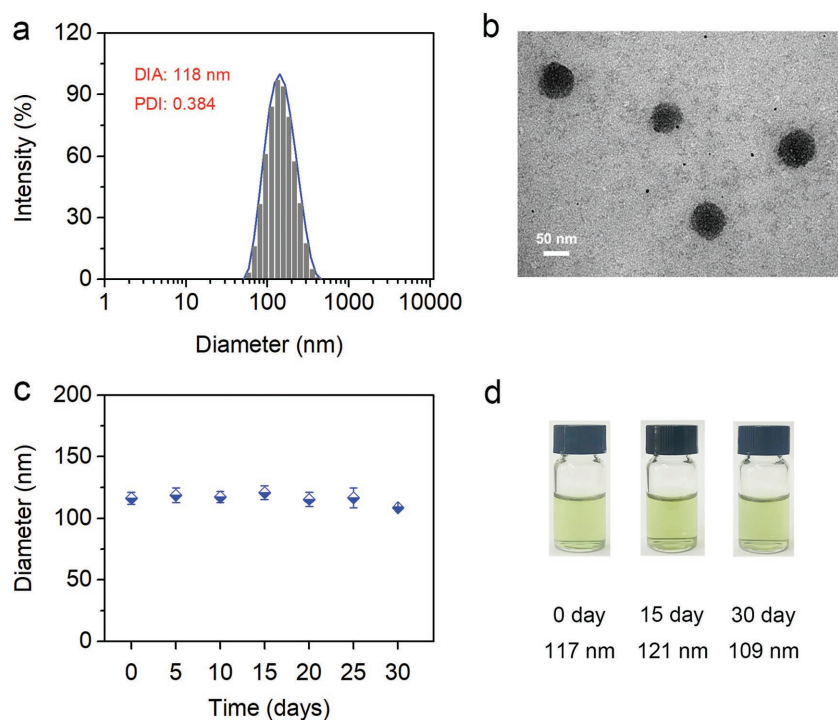


Figure 1. Size characterization and thermodynamic stability of the self-assembly with Pt-TPP-PVP₄₃₀ in aqueous solution. a) DLS measurement. b) TEM image of assembled nanoparticles. c) Average hydrodynamic diameters and d) photo images of Pt-TPP-PVP₄₃₀ (0.2 mg mL⁻¹) at different time in aqueous solution.

emission lifetime at 660 nm belongs to ultrafast nanosecond time scale with a typical fluorescent characteristic, whereas

metric hypoxia measurement capability of nanoprobe Pt-TPP-PVP₄₃₀ with the Stern–Volmer equation^[9]:

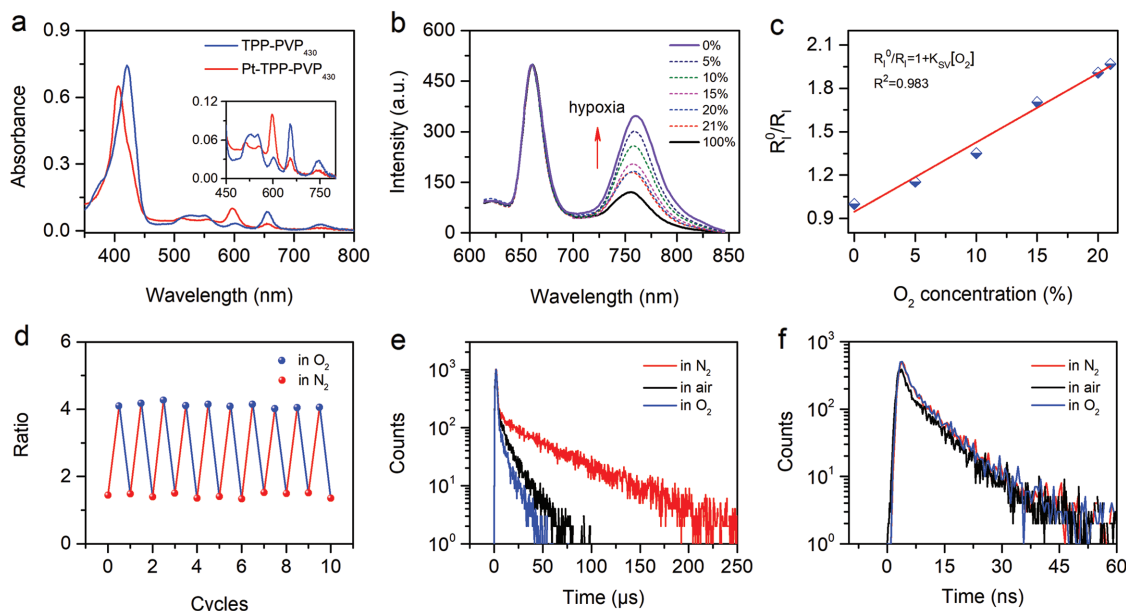


Figure 2. Optical performance of Pt-TPP-PVP₄₃₀ and its optical response to hypoxia. a) Absorption spectra of TPP-PVP₄₃₀ and Pt-TPP-PVP₄₃₀ in aqueous solution. b) Oxygen-dependent emission spectra of Pt-TPP-PVP₄₃₀ (0.2 mg mL⁻¹) in aqueous solution, $\lambda_{\text{ex}} = 595$ nm. c) Stern–Volmer plot and linear correlation of the ratiometric fluorescent/phosphorescent response to oxygen levels. d) Reversible oxygen sensing of Pt-TPP-PVP₄₃₀ in nitrogen- and oxygen-saturated aqueous solution. e) Phosphorescence decay at 760 nm and f) fluorescence decay at 660 nm of Pt-TPP-PVP₄₃₀ with different oxygen levels, $\lambda_{\text{ex}} = 405$ nm.

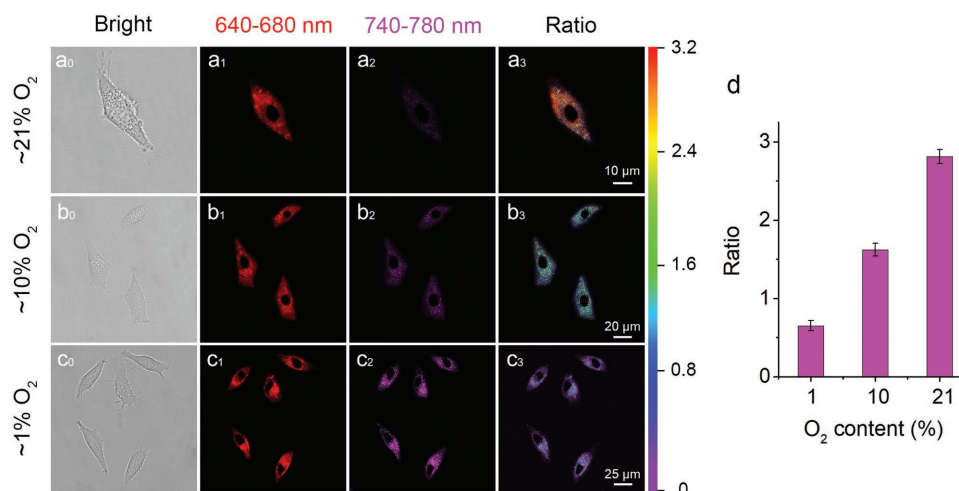


Figure 3. Ratiometric imaging of hypoxia with Pt-TPP-PVP₄₃₀ in living cells. a–c) Confocal and ratiometric images of A549 cells treated with Pt-TPP-PVP₄₃₀ (0.2 mg mL^{−1}) at different oxygen levels (≈21, ≈10, and ≈1%) for 1 h. Red channel (fluorescence) collected from 640 to 680 nm, magenta channel (phosphorescence) collected from 740 to 780 nm, and ratiometric images constructed from red and magenta channel, λ_{ex} = 595 nm. d) Ratios of averaged luminescence intensity at different oxygen levels. Error bars represent standard deviation (±SD) with *n* = 3.

$$\frac{R_I^0}{R_I} = 1 + K_{SV}[O_2] \quad (1)$$

where $R_I^0 = I_{760}^0/I_{660}^0$ and $R_I = I_{760}/I_{660}$ are the ratios of the phosphorescence intensity at 760 nm to the fluorescence intensity at 660 nm in the absence and presence of oxygen, respectively. K_{SV} is the Stern–Volmer constant, and $[O_2]$ is the oxygen concentration. As shown in Figure 2c, there is a good linear relationship between R_I^0/R_I and the oxygen level ($R^2 = 0.983$), suggesting that nanoprobe Pt-TPP-PVP₄₃₀ is capable of quantitative ratiometric sensing of hypoxia. Typically, the phosphorescence quenching by O₂ is rapidly and completely reversed by subsequent bubbling of N₂ into the nanoparticle suspension, and the ratios $I_{660\text{ nm}}/I_{760\text{ nm}}$ show negligible alteration during 10 cycles (Figure 2d), manifesting that this nanosystem can visualize the dynamics of repeated hypoxia–normoxia cycles reversibly.

Phosphorescence decay measurements provide an alternative assessment for quantification of oxygen levels.^[10] In the resulting nanoprobe Pt-TPP-PVP₄₃₀, a contrast of the phosphorescence decays at 760 nm in nitrogen, air, and oxygen-saturated solutions is displayed in Figure 2e. A phosphorescence lifetime of ≈40 μs was obtained with double-exponential decay in nitrogen-saturated solution, which was consistent with the lifetime from the reported Pt(II) porphyrin derivatives.^[11] Obviously, the phosphorescence lifetime became shortened to ≈7.96 μs in the air-saturated solution, and to ≈4.34 μs in the oxygen-saturated solution (Table S2, Supporting Information), indicative of the efficient quenching in phosphorescence emission by dissolved oxygen. In contrast, we observed the almost identical lifetime in fluorescence decay (about 7 ns, Figure 2f; Table S2, Supporting Information) at 660 nm in the above three kinds of conditions, revealing an inertness of the emission band, which acted as the perfect reference signal to oxygen.

Considering biomedical applications of probes, which are often performed in living systems such as cells, tissues, and

even in vivo with dynamic and complicated microenvironments, it is of importance to evaluate the photo-/pH-stability of nanoprobe Pt-TPP-PVP₄₃₀. We tested the photostability of the nanoprobe through monitoring its optical performance under sustained illumination with a 200 W medium pressure mercury lamp at wavelength >490 nm. After exposure to high-intensity light for 280 min, the dual emission intensities and ratios did not show striking decay during the observation period (Figure S6a, Supporting Information), indicating that the nanoprobe endows a high photobleaching threshold. Similarly, pH-dependent experiment confirmed that the probe has superior pH-resistant stability with a wide pH range from 4 to 12 (Figure S6b, Supporting Information).

Given that Pt-TPP-PVP₄₃₀ can sense oxygen level quantitatively with a unique internal reference from the specific assembled cluster fluorescent emission, we next examined its suitability for ratiometric monitoring and imaging of hypoxia in live cells with confocal microscopy. In this study, human lung carcinoma epithelial A549 cells were employed as model cells. After incubation with Pt-TPP-PVP₄₃₀ for 1 h under the normoxic condition, A549 cells afforded an intense fluorescence signal collected at wavelength from 640 to 680 nm, and negligible phosphorescence signal from 740 to 780 nm due to the quenching effect of oxygen (Figure 3a). With the decrease of oxygen levels, the fluorescence signal showed almost no fluctuation, whereas the phosphorescence signal was clearly captured in A549 cells (Figure 3b,c), which confirmed that nanoprobe Pt-TPP-PVP₄₃₀ could trace and monitor hypoxia levels in live cells. Notably, the ratiometric imaging of intracellular hypoxia was obtained from the ratio between the fluorescence and phosphorescence intensity ($I_{\text{fluor.}}/I_{\text{phos.}}$). The average ratios $I_{\text{fluor.}}/I_{\text{phos.}}$ in the cells treated with ≈21% and ≈1% O₂ concentrations were determined to be 2.8 and 0.6, respectively. An approximately fivefold decrease in ratio was observed (Figure 3d). Thus, Pt-TPP-PVP₄₃₀ is capable of quantitatively reporting the levels of hypoxia in live cells. In addition, this probe showed almost no cytotoxicity up to 6.4 mg mL^{−1} in

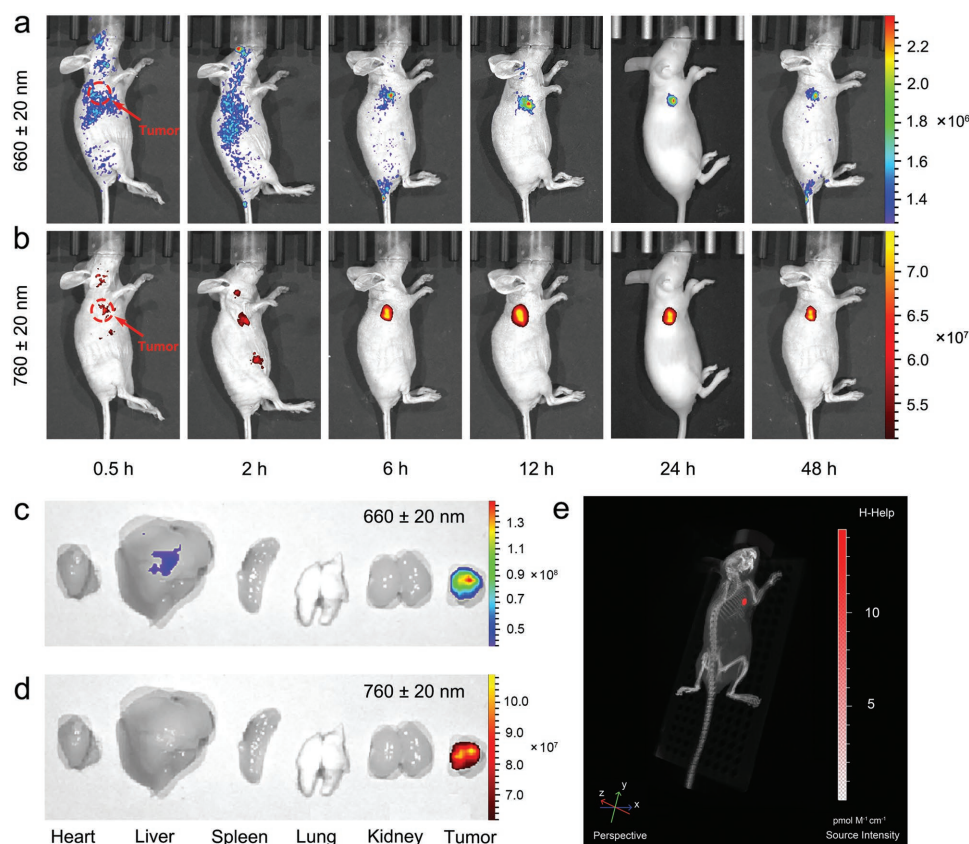


Figure 4. In vivo bioimaging of hypoxia in tumor-bearing mice at different time points after intravenous injection of Pt-TPP-PVP₄₃₀. a,b) Optical imaging windows at 660 ± 20 nm and 760 ± 20 nm, respectively. c,d) Fluorescence images of the main internal organs after anatomy with corresponding imaging windows. e) 3D in vivo bioimaging of hypoxia in tumor-bearing mice at 48 h post injection of Pt-TPP-PVP₄₃₀; $\lambda_{\text{ex}} = 595 \text{ nm}$.

MTT (3-(4,5-dimethylthiazol-2-yl)-2,5-diphenyltetrazolium bromide) assay (Figure S7, Supporting Information).

Considering the inspiring sensing and imaging of the quantitative hypoxia in live cells and its ideal NIR optical imaging window, we further investigated whether Pt-TPP-PVP₄₃₀ is proper for real-time bioimaging of tumor hypoxia in vivo. The tumor growth of A549 cell xenografts in tumor-bearing mice were administrated by intravenous and intratumoral delivery of Pt-TPP-PVP₄₃₀ (0.3 mg mL^{-1}) via the tail vein, and then scanned at different time points using an IVIS Lumina Kinetic series III imaging system (Figure 4; Figure S8, Supporting Information).

As depicted in Figure 4a, the oxygen-insensitive fluorescence signal of nanoprobe Pt-TPP-PVP₄₃₀ was clearly observed in whole body from 0.5 to 2 h post injection, and then accumulated exclusively in the tumor location during 6 to 48 h post injection, indicative of excellent tumor targeting ability possibly due to its size-dependent EPR effect. It reached a maximum level at 12 h post injection, followed by a gradual decay from 12 to 48 h post injection, thus allowing for direct visualization of the nanoprobe distribution. Upon shifting the optical imaging window from 660 ± 20 nm to 760 ± 20 nm, the oxygen-sensitive phosphorescence signal was mainly captured in tumor site with a high signal-to-noise ratio because of the minimized background interference, reduced tissue scattering in NIR region, and longer excitation wavelength. The corresponding intensities in the optical window of 760 ± 20 nm gradually

increased, and reached a maximum level at 12 h post injection (Figure 4b), such that even from the distinct enhancement the tumor could be precisely distinguished with naked eyes. For comparison, the tumor-bearing mice were also administrated with intravenous injection of small-molecular probe Pt-TPPBr ($2.9 \times 10^{-3} \text{ mg mL}^{-1}$). In sharp contrast with nanoprobe Pt-TPP-PVP₄₃₀, the phosphorescence signal from probe Pt-TPPBr was not restricted to the tumor region, and dispersed in various tissues during the 48 h post injection (Figure S9, Supporting Information). All these results demonstrated that this high selectivity tumor targeting ability of Pt-TPP-PVP₄₃₀ is attributed to the synergetic effects of prominent EPR effect, ideal NIR imaging window, fast body clearance, and hypoxia-activatable targeting ability (Figure 4; Figure S10, Supporting Information).

Moreover, to further confirm that the dual fluorescent/phosphorescent signals were from the nanoprobe accumulated in the tumor, major organs including the heart, liver, spleen, lungs, kidneys, and tumor were excised immediately at 48 h post injection, and subjected to ex vivo fluorescence imaging. In agreement with the in vivo results, both fluorescence and phosphorescence signal almost appeared at tumor tissue (Figure 4c,d). Notably, although no signals at 760 nm were detected in the liver, trace amount of nanoparticles accumulated in the liver by observation of slight signals at 660 nm (Figure 4c; Figures S10 and S11, Supporting Information). Finally, by virtue of the preferable NIR characteristic and long

excitation photon of Pt-TPP-PVP₄₃₀, we further performed 3D in vivo imaging for tumor hypoxia. High-resolution 3D in vivo image and movie were readily obtained at 48 h post administration of the nanoprobe into tumor-bearing mice (Figure 4e; Movie S1, Supporting Information). Observed from different perspectives, we found that the hypoxic tumor tissues were successfully visualized in vivo and in situ with high spatiotemporal precision. Thus, our developed technique with nanoprobe Pt-TPP-PVP₄₃₀ has successfully achieved in vivo imaging of tumor hypoxia noninvasively.

In summary, this work focuses on how to construct a ratiometric probe without conjugated internal reference moiety for avoiding energy/charge transferring interactions in traditional bischromophore-based ratiometric probes. By borrowing the nonaromatic clusteroluminescence strategy, we have developed a unique monochromophore-based ratiometric nanosensor Pt-TPP-PVP₄₃₀, which exhibits the original oxygen-sensitive Pt-TPP phosphorescence and another oxygen-insensitive fluorescence from the specific amphiphilic assembly as unprecedented inner built-in self-calibration. As demonstrated, the unique NIR fluorescent and phosphorescent emissions of Pt-TPP-PVP₄₃₀ make it highly desirable for ratiometric sensing of hypoxia levels not only in aqueous media, but also in living cells quantitatively and reversibly. To the best of our knowledge, this is the first example of monochromophore-based dual-emissive nanosensor with the specifically assembled cluster fluorescence for ratiometric hypoxia imaging, along with several advantages, such as ideal NIR imaging window, long light excitation, and suitable nanosphere morphology. Compared with the traditional bischromophore-based system, the monochromophore-based ratiometric nanosensor can avoid the undesirable energy/charge transferring interactions between the internal reference moiety and sensing chromophore. Moreover, the preferable EPR effect and long excitation wavelength in the assembly of Pt-TPP-PVP₄₃₀ can facilitate tumor targetability, and achieve a unique ratiometric assessment of hypoxia levels in living A549 cells and 3D tumor-targeting bioimaging of hypoxia in tumor-bearing mice in vivo.

Supporting Information

Supporting Information is available from the Wiley Online Library or from the author.

Acknowledgements

S.W. and K.G. contributed equally to this work. This work was supported by NSFC Science Center Program (21788102) and Creative Research Groups (21421004), National Key Research and Development Program (2016YFA0200300 and 2017YFC0906902), NSFC/China (21636002 and 21622602), National Postdoctoral Program for Innovative Talents (BX201700075), and Program of Introducing Talents of Discipline to Universities (B16017). Human lung carcinoma epithelial A549 cells were supplied by Institute of Cell Biology (Shanghai, China). This study was performed in strict accordance with the NIH guidelines for the care and use of laboratory animals (NIH Publication No. 85-23 Rev. 1985), and approved by the Institutional Animal Care and Use Committee of the National Tissue Engineering Center (Shanghai, China).

Conflict of Interest

The authors declare no conflict of interest.

Keywords

clustering-triggered emission, hypoxia sensing, monochromophore-based polymers, NIR ratiometric mode, self-assembly

Received: September 4, 2018

Revised: November 2, 2018

Published online: November 28, 2018

- [1] a) X. Huang, J. Song, B. C. Yung, X. Huang, Y. Xiong, X. Chen, *Chem. Soc. Rev.* **2018**, 47, 2873; b) J. Liu, W. Bu, J. Shi, *Chem. Rev.* **2017**, 117, 6160; c) K. Lu, T. Aung, N. Guo, R. Weichselbaum, W. Lin, *Adv. Mater.* **2018**, 30, 1707634; d) D. Wu, A. C. Sedgwick, T. Gunnlaugsson, E. U. Akkaya, J. Yoon, T. D. James, *Chem. Soc. Rev.* **2017**, 46, 7105; e) Z. Guo, Y. Ma, Y. Liu, C. Yan, P. Shi, H. Tian, W. Zhu, *Sci. China: Chem.* **2018**, 61, 1293; f) X. Li, N. Kwon, T. Guo, Z. Liu, J. Yoon, *Angew. Chem., Int. Ed.* **2018**, 57, 11522.
- [2] a) C. M. Lemon, E. Karnas, X. Han, O. T. Bruns, T. J. Kempa, D. Fukumura, M. G. Bawendi, R. K. Jain, D. G. Duda, D. G. Nocera, *J. Am. Chem. Soc.* **2015**, 137, 9832; b) C. Wu, B. Bull, K. Christensen, J. McNeill, *Angew. Chem., Int. Ed.* **2009**, 48, 2741; c) X. Zheng, X. Wang, H. Mao, W. Wu, B. Liu, X. Jiang, *Nat. Commun.* **2015**, 6, 5834; d) X. Wang, J. A. Stolwijk, T. Lang, M. Sperber, R. J. Meier, J. Wegener, O. S. Wolfbeis, *J. Am. Chem. Soc.* **2012**, 134, 17011; e) R. Xu, Y. Wang, X. Duan, K. Lu, D. Micheroni, A. Hu, W. Lin, *J. Am. Chem. Soc.* **2016**, 138, 2158; f) X. Zhou, H. Liang, P. Jiang, K. Y. Zhang, S. Liu, T. Yang, Q. Zhao, L. Yang, W. Lv, Q. Yu, W. Huang, *Adv. Sci.* **2016**, 3, 1500155; g) C. S. Hawes, T. Gunnlaugsson, *Chem* **2017**, 2, 463; h) Q. Lin, C. Bao, Y. Yang, Q. Liang, D. Zhang, S. Cheng, L. Zhu, *Adv. Mater.* **2013**, 25, 1981; i) H. Shi, X. Ma, Q. Zhao, B. Liu, Q. Qu, Z. An, Y. Zhao, W. Huang, *Adv. Funct. Mater.* **2014**, 24, 4823.
- [3] a) G. Zhang, G. M. Palmer, M. W. Dewhirst, C. L. Fraser, *Nat. Mater.* **2009**, 8, 747; b) K. Gu, Y. Xu, H. Li, Z. Guo, S. Zhu, S. Zhu, P. Shi, T. D. James, H. Tian, W. Zhu, *J. Am. Chem. Soc.* **2016**, 138, 5334; c) L. Chen, D. Wu, J. Kim, J. Yoon, *Anal. Chem.* **2017**, 89, 12596; d) C. Yin, H. Zhu, C. Xie, L. Zhang, P. Chen, Q. Fan, W. Huang, K. Pu, *Adv. Funct. Mater.* **2017**, 27, 1700493; e) J. Peng, X. Hou, F. Zeng, S. Wu, *Biosens. Bioelectron.* **2017**, 94, 278; f) Y. Huang, P. Zhang, M. Gao, F. Zeng, A. Qin, S. Wu, B. Z. Tang, *Chem. Commun.* **2016**, 52, 7288; g) A. J. Shuhendler, K. Pu, L. Cui, J. P. Uetrecht, J. Rao, *Nat. Biotechnol.* **2014**, 32, 373; h) W. Chen, Q. Huang, W. Ou, Y. Hao, L. Wang, K. Zeng, H. Guo, J. Li, Y. Liu, *Small* **2014**, 10, 1261.
- [4] a) D. Schilter, *Nat. Rev. Chem.* **2017**, 1, 0097; b) J. Mei, Y. Hong, J. W. Y. Lam, A. Qin, Y. Tang, B. Z. Tang, *Adv. Mater.* **2014**, 26, 5429; c) X. Chen, W. Luo, H. Ma, Q. Peng, W. Z. Yuan, Y. Zhang, *Sci. China: Chem.* **2018**, 61, 351; d) E. Zhao, J. W. Y. Lam, L. Meng, Y. Hong, H. Deng, G. Bai, X. Huang, J. Hao, B. Z. Tang, *Macromolecules* **2015**, 48, 64.
- [5] X. Zhou, W. Luo, H. Nie, L. Xu, R. Hu, Z. Zhao, A. Qin, B. Z. Tang, *J. Mater. Chem. C* **2017**, 5, 4775.
- [6] a) G. D. Errico, M. D. Lellis, G. Mangiapia, A. Tedeschi, O. Ortona, S. Fusco, A. Borzacchiello, L. Ambrosio, *Biomacromolecules* **2008**, 9, 231; b) J. Faria, C. Echeverria, J. P. Borges, M. H. Godinho, P. I. P. Soares, *RSC Adv.* **2017**, 7, 48972; c) P. Qiu, X. Qu, D. J. Brackett, M. R. Lerner, D. Li, C. Mao, *Adv. Mater.* **2013**,

- 25, 2492; d) Y. Kaneda, Y. Tsutsumi, Y. Yoshioka, H. Kamada, Y. Yamamoto, H. Kodaira, S. Tsunoda, T. Okamoto, Y. Mukai, H. Shibata, S. Nakagawa, T. Mayumi, *Biomaterials* **2004**, 25, 3259; e) S. P. Sullivan, D. G. Koutsonanos, M. D. P. Martin, J. W. Lee, V. Zarnitsyn, S. Choi, N. Murthy, R. W. Compans, I. Skountzou, M. R. Prausnitz, *Nat. Med.* **2010**, 16, 915.
- [7] a) P. Huang, D. Wang, Y. Su, W. Huang, Y. Zhou, D. Cui, X. Zhu, D. Yan, *J. Am. Chem. Soc.* **2014**, 136, 11748; b) C. Yan, Z. Guo, Y. Shen, Y. Chen, H. Tian, W. Zhu, *Chem. Sci.* **2018**, 9, 4959; c) X. Li, C. Kim, S. Lee, D. Lee, H. Chung, G. Kim, S. Heo, C. Kim, K. Hong, J. Yoon, *J. Am. Chem. Soc.* **2017**, 139, 10880; d) J. Liu, Q. Chen, W. Zhu, X. Yi, Y. Yang, Z. Dong, Z. Liu, *Adv. Funct. Mater.* **2017**, 27, 1605926.
- [8] a) M. Sugiuchi, J. Maeba, N. Okubo, M. Iwamura, K. Nozaki, K. Konishi, *J. Am. Chem. Soc.* **2017**, 139, 17731; b) R. Ye, Y. Liu, H. Zhang, H. Su, Y. Zhang, L. Xu, R. Hu, R. T. K. Kwok, K. S. Wong, J. W. Y. Lam, W. A. Goddard, B. Z. Tang, *Polym. Chem.* **2017**, 8, 1722.
- [9] a) O. Stern, M. Volmer, *Phys. Z.* **1919**, 20, 183; b) T. Yoshihara, Y. Yamaguchi, M. Hosaka, T. Takeuchi, S. Tobita, *Angew. Chem., Int. Ed.* **2012**, 51, 4148; c) R. Wang, H. Peng, P. Chen, L. Niu, J. Gao, L. Wu, C. Tung, Y. Chen, Q. Yang, *Adv. Funct. Mater.* **2016**, 26, 5419.
- [10] a) M. Y. Berezin, S. Achilefu, *Chem. Rev.* **2010**, 110, 2641; b) H. Kurokawa, H. Ito, M. Inoue, K. Tabata, Y. Sato, K. Yamagata, S. Kizaka-Kondoh, T. Kadonosono, S. Yano, M. Inoue, T. Kamachi, *Sci. Rep.* **2015**, 5, 10657; c) K. Y. Zhang, P. Gao, G. Sun, T. Zhang, X. Li, S. Liu, Q. Zhao, K. K. Lo, W. Huang, *J. Am. Chem. Soc.* **2018**, 140, 7827; d) A. V. Kondrashina, R. I. Dmitriev, S. M. Borisov, I. Klimant, I. O'Brien, Y. M. Nolan, A. V. Zhdanov, D. B. Papkovsky, *Adv. Funct. Mater.* **2012**, 22, 4931.
- [11] a) L. Xiao, Z. Chen, B. Qu, J. Luo, S. Kong, Q. Gong, J. Kido, *Adv. Mater.* **2011**, 23, 926; b) W. Wu, W. Wu, S. Ji, H. Guo, X. Wang, J. Zhao, *Dyes Pigm.* **2011**, 89, 199; c) E. Önal, S. Saß, J. Hurpin, K. Ertekin, S. Z. Topal, M. U. Kumke, C. Hirel, *J. Fluoresc.* **2017**, 27, 861.